

1 Frictional power dissipation in a 2 seismic ancient fault

3 Francesco Lazari^{1‡}, Angela Castagna², Stefan Nielsen³, Ashley Griffith⁴, Giorgio
4 Pennacchioni¹, Rodrigo Gomila¹, Phil Resor⁵, Chiara Cornelio⁶, Giulio Di Toro^{1,6*}

5 ¹Dipartimento di Geoscienze, Università degli Studi di Padova, Padua, Italy

6 ² Former Ph.D. student at School of Geography, Geology and the Environment, Leicester University,
7 United Kingdom.

8 ³Department of Earth Sciences, Durham University, Durham, United Kingdom

9 ⁴School of Earth Sciences, The Ohio State University, Columbus (OH), USA

10 ⁵Department of Earth and Environmental Sciences, Wesleyan University, Middletown (CT), USA

11 ⁶Sezione Roma 1, Istituto Nazionale di Geofisica e Vulcanologia, Rome, Italy

12

13 ‡Now at EPFL, Lausanne, Switzerland

14 *Corresponding author

15

16 Highlights

- 17 • Frictional power \dot{Q} [W/m²] is shear stress times slip rate during faulting
- 18 • \dot{Q} controls fault temperature increase and dynamic weakening during
19 earthquakes
- 20 • \dot{Q} cannot be estimated by seismological methods
- 21 • We use microstructural observations calibrated by experiments to estimate \dot{Q}
- 22 • \dot{Q} ranges from 4 to 60 MW/m² in an upper crustal fault patch

23

24 **Abstract**

25 The frictional power per unit area \dot{Q} (product of frictional traction τ and slip rate
26 \dot{u} in MW m⁻²) dissipated during earthquakes triggers fault dynamic weakening
27 mechanisms that control rupture nucleation, propagation and arrest. Although of
28 great relevance in earthquake mechanics, \dot{Q} cannot, with rare exceptions, be
29 determined by geophysical methods. Here we exploit theoretical, experimental and
30 geological constraints to estimate \dot{Q} dissipated on a fault patch exhumed from 7-9
31 km depth. According to theoretical models, in polymineralic, silicate rocks the
32 amplitude (< 1 mm) of the grain-scale roughness of the boundary between frictional
33 melt (pseudotachylyte) and host rock decreases with increasing \dot{Q} . The dependence
34 of grain-scale roughness with \dot{Q} is due to differential melt front migration in the host
35 rock minerals. This dependence is confirmed by friction experiments reproducing
36 seismic slip where pseudotachylytes were produced by shearing tonalite at \dot{Q}
37 ranging from 5 to 25 MW m⁻². In natural pseudotachylytes across tonalites, the grain-
38 scale roughness broadly decreases from extensional to compressional fault domains
39 where lower and higher \dot{Q} are expected, respectively. Analysis of the natural dataset
40 calibrated by experiments yields \dot{Q} values in the range of 4-60 MW m⁻² (16 MW m⁻²
41 average value). These values, estimated in small fault patches, are at the lower end
42 of broad estimates of \dot{Q} (3-300 MW m⁻²) obtained from frictional tractions (30-300
43 MPa) and fault slip rates (0.1-1 m/s) assumed as typical of upper crustal
44 earthquakes.

45 1. Introduction

46 Frictional power dissipation per unit area ($\dot{Q}(t) = \tau(t) \dot{u}(t)$ in W m^{-2} , or $\text{Nm s}^{-1}\text{m}^{-2}$ in
47 units commonly used in geodesy and seismology, with: τ frictional traction or shear
48 stress; \dot{u} on-fault slip rate) is a relevant earthquake source parameter (Sibson,
49 1980). In fact, $\dot{Q}(t)$ results in temperature increase and grain comminution in μm - to
50 cm-thick slipping zones (Sibson, 2003), that activate dynamic weakening
51 mechanisms promoting propagation of seismic ruptures (Rice, 2006; Di Toro et al.,
52 2011; Tullis et al., 2015; Pozzi et al., 2021). However, $\tau(t)$, or the absolute value of
53 frictional traction during seismic slip is transparent, with notable exceptions, to
54 measurements from the Earth's surface (Guatteri and Spudich 2006; Udias et al.,
55 2014). In fact, only the stress drop, not $\tau(t)$, has direct impact on $\dot{u}(t)$ and therefore
56 influences the seismological signature in the radiated waves (Udias et al., 2014).
57 Instead, the absolute stress levels, and hence $\tau(t) \dot{u}(t)$, could be estimated by
58 inversion analysis (1) from seismic waves if there is a visible rake rotation during
59 seismic slip (Spudich, 1992) and, (2) as recently proposed, with geodetic techniques,
60 from coseismic slip vectors measured along earthquake surface ruptures (Milliner et
61 al., 2022). However, the two above remain exceptional cases. As a consequence,
62 values of $\dot{Q}(t)$ ranging from 3 to 300 MW m^{-2} have been proposed assuming τ and \dot{u}
63 for ideal earthquakes in the continental crust and ranging from 30 to 300 MPa and
64 0.1 to 1 m s^{-1} , respectively (Fig. 2 in Sibson, 1980). In this study we aim to obtain
65 more rigorous estimates of $\dot{Q}(t)$, which controls the fault strength evolution during
66 the earthquake in the presence of thermal weakening processes, from
67 microstructural analysis of tectonic pseudotachylytes.

68 Tectonic pseudotachylytes are solidified friction melts produced during seismic
69 faulting (Sibson, 1975). Pseudotachylytes have been used to estimate several
70 earthquake source parameters, including the magnitude of frictional traction, rupture
71 directivity, slip weakening distance, energy budgets, focal mechanisms, stress drops,
72 apparent stress, fracture energy, measures of efficiency and hypocentral depths
73 (Sibson, 1975; Maddock et al., 1987; Di Toro et al., 2005; 2006; Hirose and
74 Shimamoto, 2005; Andersen et al., 2008; Pittarello et al., 2008; Beeler et al., 2016;
75 Petley-Ragan et al., 2019; Ferrand et al., 2021; Johnson et al., 2021;
76 Hosseinzadehsabeti et al., 2021). During earthquakes, seismic rupture propagation
77 (at a few km/s) induces intense and abrupt near-tip stress perturbations that result in
78 host rock fracturing, grain comminution and flash heating (Reches and Dewers,
79 2005; Rice, 2006). In silicate rocks, fault slip may result in temperature increase and
80 frictional melting of the comminuted materials and their host rocks close to the fault
81 surface (Swanson, 1992; Spray, 1995). At this stage and in the few seconds
82 following seismic slip, the melt-rock boundary migrates into the host rocks (Fialko
83 and Khazan, 2006; Nielsen et al., 2008). The melt intrudes fractures in the host rocks
84 (injection veins) or flows along the fault towards dilatational jogs and reservoirs (fault
85 veins) (Sibson, 1975). In the case of granitoid rocks, made of feldspars, quartz and
86 biotite, this ultra-fast melting occurs under non-equilibrium conditions (Shand, 1916).
87 Along the migrating melt-rock boundary, minerals with low melting temperature T_m
88 (biotite, $T_m \sim 650^\circ\text{C}$, Navrotsky, 1995) melt faster than high T_m minerals (for andesine
89 feldspar, An_{45} , and quartz, $T_m \sim 1250^\circ\text{C}$ and $T_m \sim 1730^\circ\text{C}$, respectively, Navrotsky,
90 1995; Spray, 2010). Differential mineral melting results in a grain-scale roughness of
91 the melt-rock boundary (or pseudotachylyte-host rock boundary, from now on PST-
92 HR, once the melt solidifies): embayments and protrusions form in spatial relation

93 with HR biotite and quartz/feldspar grains, respectively (Magloughlin and Spray,
94 1992, and references therein) (Fig. 1). The grain-scale roughness is related to (i)
95 mineral physical properties (T_m and thermal shock properties: Papa et al., 2018) and
96 grain size; (ii) melt temperature; and (iii) rate of the temperature increase in the
97 slipping zone, proportional to \dot{Q} . Theoretical analysis, tested by experiments on
98 gabbro, indicates that the higher the \dot{Q} , the smoother the PST-HR boundary (Nielsen
99 et al., 2010) (Fig. 1). Here we measure the grain-scale roughness of the PST-HR
100 boundary of natural pseudotachylytes within the Adamello granitoids (tonalite) along
101 the Gole Larghe Fault Zone (Italian Southern Alps; Di Toro and Pennacchioni, 2005).
102 After calibration with dedicated experiments, we estimate \dot{Q} .

103 **2. Methods**

104 Experimental pseudotachylytes were produced by shearing hollow cylinders (50/30
105 mm external/internal diameter) of non-altered Adamello tonalite with the rotary
106 machine SHIVA installed at the Istituto Nazionale di Geofisica e Vulcanologia in
107 Rome (Di Toro et al., 2010; for sample preparation see Nielsen et al., 2012). Three
108 experiments (S422, S423 and S475) were conducted at room humidity conditions,
109 target equivalent slip rates V_{eq} of 6.5 m s⁻¹ and normal stresses of 40, 20, 30 MPa,
110 respectively (Figure 2, Table 1). During the experiments, normal stress, torque
111 (converted into τ), angular rotations and speeds (converted into equivalent slip
112 distances and slip rates, respectively), and sample shortening were measured at
113 acquisition rates of 2.5 kHz (see Niemeijer et al., 2011 for details about the
114 calibration and data acquisition). We also examined a fourth pseudotachylyte
115 produced in previously published experiments performed on the same Adamello
116 tonalite. This pseudotachylyte was obtained by shearing full cylinders, 25 mm in

117 diameter, at equivalent slip rate of 1.3 m s^{-1} and 20 MPa normal stress using a rotary
118 apparatus at Kyoto University (HVR377 in Di Toro et al., 2006). The temperature
119 evolution with slip displacement in the slipping zone was estimated with 2-
120 dimensional numerical modelling (Supplementary Materials SM1, Cornelio et al.,
121 2019).

122 Natural pseudotachylytes. 22 samples were collected from eight pseudotachylyte-
123 bearing wavy faults from the dextral strike-slip Gole Larghe Fault Zone (Di Toro and
124 Pennacchioni, 2005) within the Adamello batholith (Callegari and Brack, 2002). The
125 granitoid rock (tonalite) consists of plagioclase (i.e., andesine, An_{45} , 48% modal
126 composition), quartz (29%), biotite (17%) and K-feldspar (6%) with an average grain
127 size of 2 mm (Di Toro and Pennacchioni, 2004; 2005). The fault zone was exhumed
128 from 7-9 km depth and is made of ~200 main sub-parallel, exceptionally exposed
129 faults (Di Toro and Pennacchioni, 2005; Mittempergher et al., 2021; Smith et al.,
130 2013). Pseudotachylytes were collected from extensional, neutral and compressional
131 structural domains along wavy fault veins and from injection veins (opening mode
132 cracks) (Fig. 3a). The injection veins are asymmetrically distributed and mostly
133 intruded the south-facing wall rock (Di Toro et al., 2005).

134 Thin sections. 22 natural and three experimental pseudotachylytes were cut
135 perpendicular to the slip zone and parallel to the slip direction (see Supplementary
136 Materials SM2 for the digital scans of the thin sections). The derived ~30 μm thick
137 thin sections were Syton®-polished for high resolution FESEM and EMPA analysis.

138 Microstructural analysis was performed with an optical petrographic microscope and
139 with a high-resolution Tescan Solaris Field Emission Scanning Electron Microscope
140 (FESEM) at the Dept. of Geosciences in University of Padova. Back Scatter

141 Electrons (BSE) and Cathodoluminescence (CL) imaging were performed at the
142 FESEM with operating conditions of: 14 mm working distance; 10 keV acceleration
143 voltage; and 3 nA beam current.

144 Elemental analysis (composition of the pseudotachylyte matrix) was performed with
145 electron wavelength-dispersive microprobe analysis (EMPA) on Syton®-polished thin
146 sections at the Dept. of Geosciences in University of Padova. Data were collected
147 using 15 kV as accelerating voltage and 15 nA as beam current. The analyzed
148 volume of the thin section was 2-3 μm in diameter. Sodium and potassium were
149 analyzed first to prevent alkali migration effects. The precision of the microprobe was
150 measured through the analysis of well-characterized synthetic oxide and mineral
151 secondary standards and was better than 5% for all cations.

152 Grain-scale fault roughness analysis. High resolution images (10 μm pixel) of the
153 entire thin section were obtained by optical (natural pseudotachylytes) and FESEM-
154 BSE (experimental pseudotachylytes) imaging. The PST-HR boundaries of both
155 natural and experimental pseudotachylytes were manually drawn with Inkscape®
156 over a length ranging from 6.7 to 34.5 mm and with resolution of 10 μm (see
157 Supplementary Materials SM2). The resolution of the measurements (10 μm , well
158 below the average mineral grain size, ~ 2 mm) and the length of the digitized PST-
159 HR boundaries (greater than mineral grain size) allowed us to test whether the
160 mineral grain size, together with $\dot{Q}(t)$, controls the grain-scale roughness of the PST-
161 HR boundaries. The grain-scale roughness of the PST-HR boundaries was then
162 analyzed with a MATLAB script to determine the Fast Fourier Transform (FFT)
163 spectra, ω_0 (characteristic asperity height which corresponds to the root mean

164 square, RMS, of the PST-HR boundary height) and λ_{ave} (average asperity radius),
165 defined as:

$$166 \quad \omega_0 = \sqrt{\frac{\sum_{i=1}^N z_i^2}{N}} \quad \text{Eq. 1}$$

$$167 \quad \lambda_{ave} = \frac{\sum_{i=1}^N \lambda_i}{N} \quad \text{Eq. 2}$$

168 where z_i is the height of every point i of the PST-HR boundary with respect to $z = 0$,
169 defined so that $\sum_{i=1}^N z_i = 0$ (with N the number of points along the boundary); λ_i are
170 the radii of the circles that approximate the curvature of the surface boundary around
171 the maxima of the topography (e.g., embayments) calculated from finite differences
172 at points $i-1, i, i+1$ (Nielsen et al., 2010) (Fig. 1). The roughness of the PST-HR
173 boundary is described by a series of continuous trigonometric functions where, for
174 each function, the maximum amplitude z_i is $\sqrt{2} \omega_0$ (Panzarasa & Tribulato, 1989)
175 and the length $\sqrt{2} \omega_0$ corresponds to the maximum depth of the embayments (Fig.
176 1). The MATLAB script, the thin section scans and the drawn PST-HR boundaries
177 are available at <https://researchdata.cab.unipd.it/id/eprint/725> and in Supplementary
178 Materials SM2.

179 **3. Results**

180 *3.1 Experimental pseudotachylytes*

181 In S422, S423 and S475 experiments, τ decreased from a peak value at initiation of
182 slip towards an approximately constant residual value (called “steady-state” shear
183 stress, τ_{ss}) of 2.70 MPa (at 20 MPa normal stress), 3.92 MPa (at 30 MPa) and 3.44
184 MPa (40 MPa) (Fig. 2a). These τ_{ss} correspond to \dot{Q}_{ss} ($\tau_{ss} V_{eq_{ss}}$ with $V_{eq_{ss}} = 6.5 \text{ m s}^{-1}$;
185 Fig. 2b) of 17.55, 25.50 and 22.36 MW m⁻², respectively (Table 1). HRV376

186 experiment, performed at 1.3 m s^{-1} , had $\tau_{ss} = 3.86 \text{ MPa}$ (Di Toro et al., 2006) that
187 correspond to $\dot{Q}_{ss} = 5.02 \text{ MW m}^{-2}$. In all the experiments, the PST-HR boundary is
188 similar on both sides of the slip zone, with embayments at HR biotite grains (Fig. 2c).
189 The experimental pseudotachylyte consists of abundant angularly shaped quartz
190 clasts and few rounded plagioclase clasts immersed in a uniform gray in color or, in
191 correspondence of biotite grains in the host rock, bright in color glassy-like matrix
192 (BSE-SEM images, Fig. 2d-e). Biotite clasts were not found in the pseudotachylyte
193 matrix. The most common gray in color matrix (“Ca-rich”) is enriched in Ti, Fe, Mn,
194 Mg, and K and depleted in Si, Al, Ca and Na compared to the composition of
195 plagioclase (the reverse is true of the composition of biotite) (Table 2). The less
196 common bright in color matrix (“Fe-rich”) is found next to the biotite grains in the wall
197 rocks and has a composition very similar to that of biotite (Table 2).

198

199 *3.2 Natural pseudotachylytes*

200 In many individual faults of the Gole Larghe Fault Zone, the pseudotachylytes
201 overprint cataclasites with sub-greenschists facies assemblage made of quartz,
202 plagioclase and K-feldspar clasts within a chlorite-epidote-rich matrix (Di Toro and
203 Pennacchioni, 2005; Supplementary Materials SM3). Only pseudotachylyte-bearing
204 fault segments across non-altered tonalite free of a precursor cataclasite (Di Toro et
205 al., 2006; Pittarello et al., 2008; Griffith et al., 2010) are considered here (Fig. 3). In
206 pseudotachylyte fault veins, the PST-HR boundary shows embayments at biotite
207 grains (Fig. 3b-d) and at preexisting microcracks and (pressure) dissolution seams in
208 the wall rock (Supplementary Materials SM3). Some embayments are filled by a
209 quartz-rich portion of the pseudotachylyte formed by abundant quartz clasts welded

210 by devitrified glassy matrix and microlites of biotite and plagioclase (Fig. 3b-c and
211 inset). This ultrafine aggregate is interpreted as a clast-laden melt filling the
212 embayment. However, most embayments in biotite are filled by the pseudotachylyte
213 matrix rich in biotite acicular microlites (Fig. 3d). With respect to the north-facing
214 PST-HR boundary, the southern one commonly shows (1) higher roughness (Fig.
215 3e), (2) more numerous injection veins (Di Toro et al., 2005) and, (3) more extensive
216 and scattered shattering of quartz and plagioclase grains (in contrast with discrete
217 microcracks sub-parallel to the main fault in the northern block: Fig. 3f). In injection
218 veins (Mode I cracks), the PST-HR boundaries are rougher than in fault veins (Fig.
219 3g).

220

221 *3.3 Grain-scale roughness of the pseudotachylyte-host rock (PST-HR) boundary*

222 *In experimental pseudotachylytes*, the magnitude and the slope of the FFT spectra
223 are unrelated to \dot{Q}_{ss} (Figs. 4a and c). Moreover, λ_{ave} has a weak inverse relation with
224 ω_0 (Fig. 5a) and is unrelated to \dot{Q}_{ss} (Fig. 5c) and, ω_0 decreases with increasing \dot{Q}_{ss}
225 (Fig. 5e, Table 3). This negative trend of ω_0 with \dot{Q}_{ss} is due to the high ω_0 values of
226 the grain-scale roughness of the PST-HR boundary from experiment HVR376, which
227 was performed with a much lower \dot{Q}_{ss} (5.02 MW m⁻²) than the other experiments
228 (17.55÷25.50 MW m⁻²) (Table 1). The ω_0 values plot along the FFT spectra of their
229 respective PST-HR boundaries (Fig. 4a), as expected by geometrical
230 argumentations (this is the case also for the spectra of the natural pseudotachylytes)
231 (Beeler, 2023).

232 *In natural pseudotachylytes*, the magnitude of the FFT spectra is higher in injection
233 veins and extensional domains, and lower in neutral and compressional domains

234 (Fig. 4b), the slopes of the FFT spectra are unrelated to the structural domain (Fig.
235 4d). The λ_{ave} has a weak inverse relation with ω_0 (Fig. 5b) and is unrelated to the
236 structural domain (Figs. 5d) (Table 3). The value of ω_0 is higher in the injection veins
237 than in the other structural domains with the lowest value measured in a
238 compressional domain (L05-06N) (Fig. 5f).

239 **4. Discussion**

240 We first discuss the geometry of the PST-HR boundary in both experimental and
241 natural pseudotachylytes. Then, by using the grain-scale roughness as correlating
242 factor, we estimate \dot{Q} from the samples collected in fault L05 that cuts non-altered
243 tonalite. In fact, PST-HR boundaries from natural faults with preexisting microcracks
244 and dissolution seams in their wall rocks were excluded from the analysis (see
245 Supplementary Materials SM3).

246 Experimental pseudotachylytes were produced by sliding pre-cut cylinders.
247 Therefore, the large stress perturbations expected during propagation of the seismic
248 rupture tip in natural faults (e.g., Reches and Dewers, 2005) can be assumed
249 negligible. We assume that the grain-scale roughness of experimental
250 pseudotachylytes is mainly related to preferential melting of biotite. Once “steady-
251 state” slip conditions are achieved in the experiment (Fig. 2a), the isotherms are
252 approximately fixed in space (Nielsen et al., 2008). As a consequence, the solid rock
253 specimen (1) passes through the isotherms during sample rotation, (2) heats up, (3)
254 melts, (4) the melt is expelled because of the applied normal stress and centrifugal
255 forces, and (5) the sample shortens at a constant rate (Nielsen et al., 2008) (Fig. 1).
256 Under “steady-state” conditions the temperature T_z in the host rocks can be
257 calculated by combining Eq. 4 and Eq. 70 in Nielsen et al. (2008):

258
$$T_z = (T_{melt} - T_i) \exp\left(-\frac{z\tau\dot{u}}{\kappa\rho(L+c(T_m-T_i))}\right) + T_i \quad \text{Eq. 3.}$$

259 By looking at the exponential in Eq. 3, for a given isotherm T_z , the thermal gradient in
260 the host rocks perpendicular to the fault increases with increasing \dot{Q} ($= \tau\dot{u}$). The
261 formation of embayments is controlled by preferential melting of biotite (Fig. 1). In the
262 experiments the following parameters apply: melt temperature $T_{melt} = 1450^\circ\text{C}$; rock
263 density $\rho = 2600 \text{ kg/m}^3$; latent heat $L = 3.32 * 10^5 \text{ J/kg}$ (Di Toro and Pennacchioni,
264 2006); ambient temperature $T_i = 20^\circ\text{C}$; thermal diffusivity $\kappa = 5 * 10^{-7} \text{ m}^2/\text{s}$ for the
265 temperature range 650-1450°C of host rock melting (considering the nominal melting
266 temperature of biotite as the lower end and the melt temperature as the higher end
267 of this temperature range; Whittington et al., 2009); and specific heat capacity $c =$
268 1500 J/kg/K (Waples and Waples, 2004).

269 In the experiments presented here, the temperature in the slip zone during frictional
270 sliding was not measured because of technical limitations of the most used
271 techniques (e.g., high speed infra-red camera or thermocouples, see discussion in
272 Aretusini et al., 2021). However, the estimated melt temperature of 1450°C is
273 consistent with the microstructural observations (Fig. 2d-e) and with the chemical
274 composition of the pseudotachylyte glass (Table 2). In fact, (1) though the host rock
275 tonalite is made by 49% plagioclase (An_{45}), 29% quartz, 16% biotite and 6% K-
276 feldspar, the clasts that survived from melting are mostly made of quartz (melting
277 point 1730°C), while there are few plagioclase An_{45} clasts (melting point 1250°C,
278 Spray, 2010; Deer et al., 1992) and none of biotite (Fig. 2d) and (2) melting of biotite
279 and plagioclase melting largely contributes to the formation of the friction melt (see
280 rounding of plagioclase grains and incipient melting of biotite in Figs.2d-e). This
281 interpretation is supported by the elemental composition of the glassy matrix which

282 has a SiO₂ concentration slightly lower than the one of plagioclase but higher than
283 that of biotite and by the presence of FeO, K₂O, CaO, MgO, etc. which is consistent
284 with selective melting of plagioclase and biotite (and probably K-feldspar) (Table 2).
285 We infer that the frictional melt temperature was larger than the melting point of
286 plagioclase (1250°C estimated from the solidus of plagioclase melting T at ambient
287 pressure for An₄₅ content, see Deer et al., 1992 and references therein) but lower
288 than that of quartz (1730°C, Navrotsky, 1995). The above temperature estimates, in
289 the range of 1450°C and constrained by microstructural observations and
290 geochemical investigations, are in the range of temperature estimates obtained from
291 numerical models (Supplementary Materials SM1). The temperature increase in the
292 slip zone due to shear heating was estimated using Finite Element Analysis to solve
293 time dependent thermal diffusion in 2 dimensions (Cornelio et al., 2019). In the
294 model, the heat source is the measured $\tau(t) V_{eq}(t)$ and it is assumed that all the
295 mechanical energy is dissipated as heat, a condition that appears to be satisfied in
296 this experimental configuration (Niemeijer et al., 2011; Aretusini et al., 2021).
297 According to numerical modeling results, temperatures of at least 1450°C were
298 reached in all experiments, and for longer times in experiments performed with
299 higher \dot{Q}_{ss} (Fig. SM1).

300 Lastly, we introduce $z = \sqrt{2} \omega_0$, with ω_0 calculated for each experimental PST-HR
301 boundary. The length $\sqrt{2} \omega_0$ is the distance of the bottom of the embayments from
302 the reference plane $z = 0$ and should correspond to the maximum penetration depth
303 of the isotherm responsible for biotite melting (Fig. 1). Therefore, from Eq. 3, the
304 effective melting temperature of biotite is $T_{m\,eff} = 870^\circ\text{C} \pm 180^\circ\text{C}$. This $T_{m\,eff}$ is
305 higher than the value $T_m = 650^\circ\text{C}$ reported in the literature (Navrotsky, 1995). There

306 are several possible explanations for this discrepancy. One is that because of
307 kinetics effects, during the short time of the coseismic frictional heat pulse, biotite is
308 not melted down to its nominal melting temperature T_m , but to a higher temperature
309 $T_{m\,eff}$. A second explanation is related to the tribo-mechanical processes
310 responsible for the formation and evolution of grain-scale roughness. For instance,
311 (1) frictional melting may include more complex poly-phase quasi-equilibrium melting
312 processes at the asperity scale (Lee et al., 2017) or, (2) the higher asperities made
313 of quartz or feldspar may undergo continuous frictional wear, particularly where the
314 friction melt is freely extruded and melt layer is thus thin. These two tribo-mechanical
315 processes contribute to smoothing the grain-scale roughness by melting or wearing
316 out those minerals that have a higher individual melting point than biotite. Therefore,
317 the assumption that the grain-scale roughness of experimental pseudotachylytes is
318 related only to preferential melting of biotite at $T_m = 650^\circ\text{C}$ should be relaxed to
319 include other micro-scale processes. In any case, the contribution of these second-
320 order tribo-mechanical processes in defining the grain-scale roughness does not
321 substantially alter the outcomes of our analysis as discussed below.

322 In natural pseudotachylyte-bearing faults, the extensional, neutral and compressional
323 structural domains should correspond to domains of low, intermediate and high
324 normal (effective) stresses σ_n , respectively. The nearby domains of fault L05 (Fig.
325 3a) should have recorded a similar slip history under comparable average coseismic
326 slip rates (Griffith et al., 2010). When the fault is lubricated by friction melts, the
327 frictional traction τ and, therefore, \dot{Q} are expected to be higher in the compressional
328 structural domains ($\tau \propto \sigma_n^{0.25}$, Nielsen et al., 2008) than in neutral and extensional
329 ones. In the case of injection veins (mode I cracks) the frictional traction is negligible
330 and the PST-HR boundary should be mainly affected by fracturing and by melt-rock

331 interaction. In fact, in injection veins the melt temperature is independent of the
332 frictional power (here, $\dot{Q} = 0$) and, the melt, once injected, cools slowly to ambient
333 temperature as the melting front propagates in the wall rocks ("*Stefan problem*", Ch.
334 XI in Carslaw and Jaeger, 1959). This type of melt-rock interaction results in a lower
335 temperature gradient in the wall rocks and in a higher grain-scale roughness at the
336 PST-HR boundary. Consistent with this interpretation, the ω_0 values are
337 systematically higher in injection veins than in fault veins (Fig. 5f). In fault veins, the
338 grain-scale roughness of the PST-HR boundary is affected by:

339 1. Asymmetric and intense damage associated with the transient stress
340 perturbation during the propagation of the seismic rupture front at some km s^{-1}
341 (Poliakov et al., 2002). For eastward propagating ruptures of the Gole Larghe
342 right-lateral strike slip faults, stress perturbation induced intense fracturing
343 and wall-rock spallation especially in the southern block of individual faults (Di
344 Toro et al., 2005) (Fig. 3f bottom). In contrast, the orientation of the
345 microcracks in the northern wall rock is sub-parallel to the E-W strike of the
346 fault (Fig. 3f top). This orientation is consistent with the direction of the
347 maximum transient compressive stress associated with eastward rupture
348 propagation along a right-lateral strike slip fault (Fig. 4 in Di Toro et al., 2005).
349 According to this interpretation, the northern and southern blocks were
350 located on the transient compression and tension stress fields, respectively, of
351 the ancient rupture that propagated along this fault segment. The grain-scale
352 roughness resulting from the stress perturbation at the rupture-tip is not
353 included in the theoretical model which relates the grain-scale roughness to \dot{Q}
354 (Nielsen et al., 2010);

- 355 2. Reworking of the PST-HR boundary due, for instance, to filling of
356 embayments by the clasts carried by the melt (Figs. 3b-c). The resulting grain-
357 scale roughness should be excluded from our analysis (see black in color line
358 in Fig. 3b).
- 359 3. Preferential melting of biotite with respect to the other host rock-forming
360 minerals due to non-equilibrium frictional melting. This would result in the
361 grain-scale roughness related to the \dot{Q} in the process zone that is considered
362 in the theoretical analysis by Nielsen et al. (2010). We note here that grain-
363 scale roughness will thus reflect not only the heating rate of the slipping zone
364 and the associated thermal gradient in the wall rocks but also the relative
365 melting points of the various mineral phases and their grain sizes. We make
366 also the assumption that steady-state conditions during frictional melting were
367 achieved. This assumption might be partly relaxed by the evidence that in the
368 selected natural faults the pseudotachylyte matrix at the contact with the
369 biotite grains in the wall rock includes biotite microlites precipitated from the
370 melt (Fig. 3d). In addition, the embayments are laterally confined by well-
371 rounded plagioclase grains (Fig. 3d). The above microstructural evidence is
372 consistent with progressive migration of the isotherms and associated melting
373 front in the wall rock tonalite (Fig. 1), followed by crystallization of biotite
374 microlites during cooling and solidification of the melt (Fig. 3d).

375 Based on the above analysis of the physical processes that shape the PST-HR
376 boundary, we decided to use ω_0 to estimate \dot{Q} within the several parameters
377 (magnitude and slope of FTT, ω_0 and λ_{ave}) that describe the grain-scale roughness
378 (Table 3). In fact, the FFT magnitude of the PST-HR boundary is affected by \dot{Q} only
379 in the natural pseudotachylytes (Figs. 4a-b). Instead, the slope of the FFT is a

380 measure of roughness scaling across the scale of measurements (10 μm – 10's of
381 mm) and thus is not necessarily affected by \dot{Q} (Beeler, 2023). Moreover, there is not
382 a clear dependence of λ_{ave} with \dot{Q} or the structural domain (Figs. 5c-d). In fact, while
383 the value of ω_0 represents the roughness at the profile scale (6.7÷34.5 mm)
384 spanning ~3-17 grains and may thus be particularly sensitive to grain-scale
385 roughness, λ_{ave} is a local measure comparing neighboring profile points (across 30
386 μm), which is much smaller than the grain scale. The poor dependence of λ_{ave} with
387 \dot{Q} is due to the fact that melting along sliding surfaces is the primary driver of the
388 grain-scale roughness, and, consequently, λ_{ave} depends on both grain size and
389 melting point of the individual minerals. Since the tonalites discussed here that host
390 the natural and experimental pseudotachylyte have the same average grain size,
391 λ_{ave} is poorly dependent of \dot{Q} . In contrast, ω_0 , although like λ_{ave} varies with grain size
392 and melting point of the host rock minerals (e.g., the maximum value of ω_0 will be
393 limited by the size of the mineral with the lowest melting point), it depends also on
394 the heating rate of the slipping zone and the associated thermal gradient in the wall
395 rocks, which are proportional to \dot{Q} (Fig. 1).

396 Because of the effect of the processes listed at points 1 and 2 above, to estimate \dot{Q}
397 we consider the northern PST-HR boundary of the samples from fault L05. In these
398 pseudotachylytes, (1) there is no evidence for sub-greenschists facies cataclastic
399 precursors (Fig. 3), and (2) the northern block was less affected by the coseismic
400 stress perturbation because located in the compression field of the eastward
401 propagating rupture (Fig. 3f, see Di Toro et al., 2005). We can reasonably assume
402 that in these samples the grain-scale roughness is mainly related to the preferential
403 melting of biotite (Fig. 3d). From the analysis of the experimental pseudotachylytes

404 the calculated melting temperature for biotite is assumed to be $T_{meff} = 870\text{ }^{\circ}\text{C}$ (Fig.
405 5e); substituting it as T_z in Eq. 3 and rearranging the equation we obtain:

$$406 \quad \tau \dot{u} = \frac{\kappa \rho (L + c(T_m - T_i))}{\sqrt{2} \omega_0} \ln \left(\frac{T_m - T_i}{870^{\circ}\text{C} - T_i} \right) \quad \text{Eq. 4}$$

407 where $T_i = 250^{\circ}\text{C}$ is ambient temperature during seismic faulting (Di Toro and
408 Pennacchioni, 2006). The estimated \dot{Q} ($\tau \dot{u}$) for the natural pseudotachylytes of the
409 northern boundary of fault L05 are reported in Fig. 6. On this diagram, we also plot
410 the ω_0 vs. \dot{Q} measurements for the experimental pseudotachylytes. According to this
411 analysis, natural pseudotachylytes are the result of \dot{Q} ranging from 4 to 60 MW m^{-2} ,
412 with an arithmetic mean value of 16 MW m^{-2} .

413 These first \dot{Q} estimates obtained from field and microstructural observations are in
414 the lower range of the broad \dot{Q} range from 3 to 300 MW m^{-2} proposed in the literature
415 (Fig. 2 in Sibson, 1980). But these latter estimates were based on a range of
416 possible coseismic shear stress ($30 < \tau < 300\text{ MPa}$) and on-fault slip rate ($0.1 < \dot{u} <$
417 1.0 m/s) achieved at crustal seismogenic depths of about 10 km (i.e., these
418 hypocentral depths are about the same as in our study). The proposed \dot{Q} estimates
419 of $> 100\text{ MW m}^{-2}$ would have been excessive because they would have induced very
420 high temperatures in the slip zone ($> 10.000^{\circ}\text{C}$), unless a relevant reduction in τ
421 during coseismic slip was considered (see Fig 4 in Sibson, 1980). Though our field
422 estimates of \dot{Q} (mean value 16 MW m^{-2}) were determined in a fault patch and may
423 not be representative of the entire fault, they are supported by experimental
424 evidence and are in agreement with the hypothesis by Sibson (1980) of large
425 reduction in τ during seismic slip (Fig. 2a). In addition, the estimates of \dot{Q} proposed
426 here are based on microstructural observations associated with the effects of

427 temperature increase in the slip zone (Figs. 1-3) rather than on approximate
428 estimates of deformation conditions during coseismic slip.

429 **5. Conclusions**

430 What is the magnitude of the frictional power (\dot{Q}) dissipated on a fault during an
431 earthquake? We address this question by exploiting a theoretical model which
432 relates the grain-scale roughness of the pseudotachylyte-host rock boundary
433 described by the characteristic asperity height ω_0 to \dot{Q} (Nielsen et al., 2010) (Fig. 1).
434 In experimental pseudotachylytes produced under known \dot{Q} (Fig. 2), ω_0 decreases
435 with increasing \dot{Q} (Fig. 5e), as predicted by the model (Fig. 1). In natural
436 pseudotachylytes from the Gole Larghe Fault Zone within the Adamello tonalites, ω_0
437 is higher for injection veins (where \dot{Q} should be negligible) than for extensional,
438 neutral and compressional fault domains (Fig. 5f). These domains should correspond
439 to low, intermediate and high \dot{Q} , respectively (Figs. 5e-f). Contrary to experimental
440 pseudotachylytes, produced by shearing pre-cut samples, the grain-scale roughness
441 of natural pseudotachylyte PST-HR boundary is also affected by the intense damage
442 associated with the propagation of the seismic rupture tip. In the Gole Larghe Fault
443 Zone, this host rock damage is especially developed in the southern wall block.
444 Therefore, to estimate \dot{Q} we considered six samples of the northern boundary of fault
445 L05. In fact, the interpretation of the microstructures (Fig. 3) suggests that the grain-
446 scale roughness of the northern side of fault L05 mainly resulted from preferential
447 melting of biotite (Fig. 3d). From the experimental dataset we estimate with Eq. 3 the
448 (effective) melting temperature $T_{m\,eff} = 870^\circ\text{C}$ of biotite during frictional melting. This
449 estimate is based on the depth $z = \sqrt{2} \omega_0$ of the embayments, which should
450 correspond to the maximum penetration depth of the isotherm responsible for biotite

451 melting. Finally, by inserting $z = \sqrt{2} \omega_0$ in Eq. 4 for the samples from fault L05, we
452 estimate \dot{Q} which ranges from 4 to 60 MW m⁻², with an average value of 16 MW m⁻².
453 These \dot{Q} values are in the lower range of very broad estimates (3-300 MW m⁻²)
454 based on typical average seismic slip rates and frictional tractions inferred for the
455 upper continental crust (Sibson, 1980). In addition, these low estimates of \dot{Q} would
456 suggest that the pseudotachylytes studied, at least at the scale of the fault patch
457 investigated (a few m²), may be representative of earthquakes that have excess
458 radiated seismic energy (Beeler et al., 2016). Actually, our estimates of \dot{Q} based on
459 field and microstructural observations, although valid for fault patches of few m² in
460 size, could be compared with \dot{Q} values obtained in the rare cases where absolute
461 stress levels, and hence $\tau(t) \dot{u}(t)$, can be estimated (Spudich, 1992; Milliner et al.,
462 2022). However, our field-based estimates of frictional power per unit area
463 dissipated during earthquakes, although independent of assumptions about the
464 magnitude of seismic slip rates and shear tractions, may suffer from a number of
465 other assumptions as discussed above. For instance, the theoretical model does not
466 include (1) non-steady-state conditions and second order effects (e.g., latent heat of
467 melting, mineral and temperature-dependent thermal conductivity variations) which
468 may perturb the curvature of the isotherms migrating in the wall rocks (i.e., we
469 assumed planar isotherms in Fig. 1) or (2) other tribo-mechanical processes that
470 may contribute to the shaping of the grain-scale roughness. Nevertheless, the
471 approach presented here can be applied to pseudotachylytes produced in other
472 geodynamic settings and at deeper crustal levels and will help determine this
473 relevant but elusive parameter of the earthquake source.

474 Acknowledgements

475 GDT and SN acknowledge the ERC StG USEMS (205175) and CoG NOFEAR
476 (614705) projects, RG the European Union Marie Skłodowska-Curie project
477 FRICTION (896346), GP and GDT the PRIN 2022 project THALES, and PR NSF
478 EAR-1145238. Leonardo Tauro is thanked for thin section preparation. All authors
479 thank Romano Ceschin from the Rifugio Ai Caduti dell'Adamello for his generous
480 hospitality. Rebecca Bendick (EPSL Editor), Nicholas Beeler and an anonymous
481 reviewer are thanked for their suggestions and constructive comments.

482 Contributions

483 **F. Lazari:** Conceptualization, Writing - Original Draft, Methodology, Software, Formal
484 analysis, Investigation, Data Curation. **A. Castagna:** Conceptualization, Writing -
485 Review & Editing, Methodology, Software, Formal analysis, Investigation, Data
486 Curation. **S. Nielsen:** Conceptualization, Writing - Review & Editing, Software,
487 Investigation, Resources, Funding acquisition. **A.W. Griffith:** Conceptualization,
488 Writing - Review & Editing, Methodology, Software. **G. Pennacchioni:** Writing -
489 Review & Editing, Investigation, Resources, Funding acquisition. **R. Gomila:**
490 Methodology, Writing – Review & Editing, Resources. **P. Resor:** Writing - Review &
491 Editing, Methodology, Investigation, Funding acquisition. **C. Cornelio:** Review &
492 editing, thermal modelling. **G. Di Toro:** Conceptualization, Writing - Review &
493 Editing, Methodology, Investigation, Resources, Supervision, Project administration,
494 Funding acquisition.

495

496 References

- 497 Andersen, T.B., Mair, K., Austrheim, A., Podladchikov Y., Vrijmoed J.C., 2008. Stress
498 release in exhumed intermediate and deep earthquakes determined from
499 ultramafic pseudotachylyte. *Geology* 36, 995–998.
- 500 Aretusini S., Núñez-Cascajero A., Spagnuolo E., Tapetado A., Vázquez C., Di Toro
501 G., 2021. Fast and localized temperature measurements during simulated
502 earthquakes in carbonate rocks. *Geophys. Res. Lett.* 48, e2020GL091856,
503 <https://doi.org/10.1029/2020GL091856>
- 504 Beeler, N., Di Toro, G., Nielsen, S., 2016. Earthquake source properties from
505 pseudotachylite. *Bull. Seism. Soc. Am.* 106, 2764-2776.
- 506 Beeler, N., 2023. On the scale-dependence of fault surface roughness. *J. Geophys.*
507 *Res.* <https://doi.org/10.1029/2022JB024856>
- 508 Callegari, E., Brack, P., 2002. Geological map of the Tertiary Adamello batholith
509 (Northern Italy) Explanatory notes and legend. *Mem. Sci. Geol.* 54, 19–49.
- 510 Carslaw, H.S., Jaeger, J.C., 1959. *Conduction of Heat in Solids*, 2nd edition. Oxford at
511 the Clarendon Press, Oxford.
- 512 Cornelio C., Spagnuolo E., Di Toro G., Nielsen S., Violay M., 2019. Mechanical
513 behaviour of fluid-lubricated faults. *Nature Communications*, 10.1038/s41467-019-
514 09293-9, pp. 1-7.
- 515 Deer W.A., Howie, R.A., Zussman, J., 1992. *An introduction to rock-forming minerals*.
516 2nd Ed. Longman Scientific & Technical, Harlow (UK).

- 517 Di Toro, G., Pennacchioni, G., 2005. Fault plane processes and mesoscopic structure
518 of a strong-type seismogenic fault in tonalites (Adamello batholith, Southern Alps).
519 *Tectonophysics* 402, 55–80.
- 520 Di Toro, G., Nielsen, S., Pennacchioni, G., 2005. Earthquake rupture dynamics frozen
521 in exhumed ancient faults. *Nature* 436, 1009–1012.
- 522 Di Toro, G., Hirose, T., Nielsen, S., Pennacchioni, G., Shimamoto T., 2006. Natural
523 and experimental evidence of melt lubrication of faults during earthquakes.
524 *Science* 311, 647–649.
- 525 Di Toro, G., Niemeijer, A., Tripoli, A., Nielsen, S., Di Felice, F., Scarlato, P., Spada,
526 G., Alessandrini, R., Romeo, G., Di Stefano, G., Smith, S., Spagnuolo, E.,
527 Mariano, S., 2010. From field geology to earthquake simulation: a new state-of-
528 the-art tool to investigate rock friction during the seismic cycle (SHIVA).
529 *Rendiconti Lincei* 21, pp. 95–114.
- 530 Di Toro, G., Han, R., Hirose, T., De Paola, N., Nielsen, S., Mizoguchi, K., Ferri, F.,
531 Cocco, M., Shimamoto, T., 2011. Fault lubrication during earthquakes. *Nature*
532 471, 494–499.
- 533 Ferrand, T. P., Nielsen, S., Labrousse, L., Schubnel, A., 2021. Scaling seismic fault
534 thickness from the laboratory to the field. *J. Geophys. Res.* 126, e2020JB020694.
- 535 Fialko, Y., Khazan, Y., 2005. Fusion by the earthquake fault friction: stick or slip? *J.*
536 *Geophys. Res.* 110, B12407.
- 537 Griffith, W. A., Nielsen, S., Di Toro, G., Smith S.A.F., 2010. Rough faults, distributed
538 weakening, and off-fault deformation. *J. Geophys. Res.* 115, B08409.

539 Guatteri, M., Spudich P., 1998. Coseismic temporal changes of slip direction: The
540 effect of absolute stress on dynamic rupture. *Bull. Seism. Soc. America* 88, 777–
541 789.

542 Hirose, T., Shimamoto, T., 2005. Slip-weakening distance of faults during frictional
543 melting as inferred from experimental and natural pseudotachylytes. *Bull. Seism.*
544 *Soc. America* 95, 1666–1673.

545 Hosseinzadehsabeti, E., Ferré, E.C., Andersen, T. B., Geissman, J. W., Bilardello, D.,
546 Di Toro, G., 2021. Focal mechanisms of intraslab earthquakes: Insights from
547 pseudotachylytes in mantle units. *J. Geophys. Res.*, e2020JB021479.

548 Johnson, S. E., Song, W. J., Vel, S. S., Song, B. R., Gerbi, C. C., 2021. Energy
549 partitioning, dynamic fragmentation, and off-fault damage in the earthquake
550 source volume. *J. Geophys. Res.* 126, e2021JB022616.

551 Lee, S.K., Han, R., Jeong, G.Y., Khim, H., Hirose., T., 2017. Quasi-equilibrium melting
552 of quartzite upon extreme friction. *Nature Geoscience* 10, 436-442.

553 Maddock, R.H., Grocott, J., Van Nes, M., 1987. Vesicles, amygdales and similar
554 structures in fault-generated pseudotachylytes. *Lithos* 20, 419-432.

555 Magloughlin, J.F., Spray, J.G., 1992. Frictional melting processes and products in
556 geological materials: introduction and discussion. *Tectonophysics* 204, 197-206.

557 Milliner, C. W. D., Aati, S., Avouac, J. 2022. Fault friction derived from fault bend
558 influence on coseismic slip during the 2019 Ridgecrest Mw 7.1 mainshock. *J.*
559 *Geophys. Res.* 127, e2022JB024519.

560 Mitterpergher, S., Zanchi, A., Zanchetta, S., Fumagalli, M., Gukov, K., Bistacchi, A.,
561 2021. Fault reactivation and propagation in the northern Adamello pluton: The

562 structure and kinematics of a kilometre-scale seismogenic source. *Tectonophysics*
563 806, 228790.

564 Navrotsky, A., 1995. Thermodynamic properties of minerals. In: *Rock Physics and*
565 *Phase Relations. A Handbook of Physical Constants. AGU Reference Shelf 2*, pp.
566 18–32.

567 Nielsen, S., Di Toro, G., Hirose, T., Shimamoto T., 2008. Frictional melt and seismic
568 slip. *J. Geophys. Res.* 113, B01308.

569 Nielsen, S., Di Toro, G., Griffith W.A., 2010. Friction and roughness of a melting rock
570 surface. *Geophys. J. Int.* 182, 299 –310.

571 Nielsen, S., Spagnuolo, E., Violay, M., 2012. The ultimate sample preparation for
572 rotary shear experiments. *Rapporti tecnici INGV*, /[http://istituto.ingv.it/l-ingv/
573 produzione-scientifica/rapporti-tecnici-ingv/numeri-pubblicati-2012S](http://istituto.ingv.it/l-ingv/produzione-scientifica/rapporti-tecnici-ingv/numeri-pubblicati-2012S).

574 Niemeijer, A., Di Toro, G., Nielsen, S., Di Felice F., 2011. Frictional melting of gabbro
575 under extreme experimental conditions of normal stress, acceleration, and sliding
576 velocity, *J. Geophys. Res.* 116, B07404.

577 Panzarasa, G., Tribulato, S., 1989. *Serie di funzioni*. Edizioni Tecnos Milano, pp. 124.

578 Papa, S., Pennacchioni, G., Ross, J.A., Faccenda, M., 2018. The fate of garnet during
579 (deep-seated) coseismic frictional heating: the role of thermal shock. *Geology* 46,
580 471-474.

581 Petley-Ragan, A., Ben-Zion, Y., Austrheim H., Ildefonse, B., Renard, F., Jamtveit, B.,
582 2019. Dynamic earthquake rupture in the lower crust. *Science Advances* 5,
583 eaaw0913, 1-7.

584 Pittarello L., Di Toro, G., Bizzarri, A., Pennacchioni, G., Hadizadeh, J., Cocco, M.,
585 2008. Energy partitioning during seismic slip in pseudotachylyte-bearing faults
586 (Gole Larghe Fault, Adamello, Italy). *Earth Planet. Sci. Lett.* 269, 131-139.

587 Poliakov, A.N..B., Dmowska, R., Rice, J.R., 2002. Dynamic shear rupture interactions
588 with fault bends and off-axis secondary faulting. *J. Geophys. Res.* 107 (B11),
589 2295.

590 Pozzi, G., De Paola, N., Nielsen, S.B., Holdsworth, R. E., Tesei, T., Thieme, M.,
591 Demouchy, S., 2021. Coseismic fault lubrication by viscous deformation. *Nature*
592 *Geosciences* 14, 437–442.

593 Reches, Z., Dewers T.A., 2005. Gouge formation by dynamic pulverization during
594 earthquake rupture. *Earth Planet. Sci. Lett.* 235, 361– 374.

595 Rice, J. R., 2006. Heating and weakening of faults during earthquake slip. *J. Geophys.*
596 *Res.* 111, B05311.

597 Shand, S.J., 1916. The pseudotachylyte of Parijs (Orange Free State) and its relation
598 to “trap-shotten gneiss” and “flinty crush rock”. *Q. J. Geol. Soc. Lon.* 72, 198-221.

599 Sibson, R. H., 1975. Generation of pseudotachylyte by ancient seismic faulting.
600 *Geophys. J. R. Astron. Soc.* 43, 775–794.

601 Sibson, R. H., 1980. Power dissipation and stress levels on faults in the upper crust. *J.*
602 *Geophys. Res.* 85, 6239–6247.

603 Sibson, R.H., 2003. Thickness of the seismic slip zone. *Bull. Seism. Soc. Am.* 93, pp.
604 1169-1178.

605 Smith, S. A. F., Bistacchi, A., Mitchell, T.M., Mittempergher, S., Di Toro G., 2013. The
606 structure of an exhumed intraplate seismogenic fault in crystalline basement.
607 *Tectonophysics* 599, 29–44.

608 Spray, J.G., 1995. Pseudotachylyte controversy: Fact or friction? *Geology* 23, 1119-
609 1122.

610 Spray, J. G., 2010. Frictional melting processes in planetary materials: from
611 hypervelocity impact to earthquakes”. *Ann. Rev. Earth Plan. Sci.* 38, 221–254.

612 Spudich, P., 1992. On the inference of absolute stress levels from seismic radiation,
613 *Tectonophysics*, 211, 99-106.

614 Swanson, M. T., 1992. Fault structure, wear mechanisms and rupture processes in
615 pseudotachylyte generation. *Tectonophysics* 204, 223–242.

616 Tullis T.E. 2015. Mechanisms for friction of rock at earthquake slip rates. In *Treatise*
617 *on Geophysics*, 2nd Edition, Ed. Kanamori H., vol. 4, pp.139-159, Elsevier.

618 Udias A., Madariaga R., Buforn E., 2014. *Source mechanism of earthquakes: Theory*
619 *and practice*. Cambridge University Press.

620 Waples D.W., Waples J.S., 2004. A review and evaluation of specific heat capacities
621 of rocks, minerals, and subsurface fluids. Part 1: Minerals and Nonporous Rocks.
622 *Natural Resources Research*, 13, 97-122.

623 Whittington A.G., Hofmeister A.M., Nabelek P.I., 2009. Temperature-dependent
624 thermal diffusivity of the Earth’s crust and implications for magmatism. *Nature*
625 458, 319-321.

626

627 Figure & Tables Captions

628 **Figure 1:** *Conceptual model of the relation between frictional power dissipation*
629 *(\dot{Q}) and grain-scale roughness of the boundary between melt (PST, pseudotachylyte*
630 *once solidified) and host rock (HR) during seismic slip in a granitoid (Qz = quartz:*
631 *$T_m \sim 1730^\circ\text{C}$; Bt = biotite: $T_m \sim 650^\circ\text{C}$; Pl = plagioclase An_{45} : $T_m \sim 1250^\circ\text{C}$; Navrotsky,*
632 *1995; Spray, 2010; Deer et al., 1992). Red lines represent isotherms with decreasing*
633 *spacing with increasing \dot{Q} . (a) High \dot{Q} : the thermal gradient is high; the host rock*
634 *minerals melt almost at the same rate resulting in a relatively smooth PST-HR*
635 *boundary. (b) Low \dot{Q} : the thermal gradient is low and biotite is more affected by*
636 *melting than the other minerals; as result deep embayments (Emb) and a rugged*
637 *PST-HR boundary develop. The grain-scale roughness of the PST-HR boundary is*
638 *described by ω_0 (characteristic asperity height, Eq. 1) and λ_{ave} (average radius of*
639 *the asperities, Eq. 2). The distance $z = \sqrt{2} \omega_0$ corresponds to the depth of the*
640 *embayments (see also methods section). In this conceptual model, the thermal*
641 *diffusivity of melt and wall rocks is the same and latent heat of fusion is not*
642 *considered; the isotherms are approximated as planes for simplicity. In reality,*
643 *different thermal diffusivities and the latent heat of fusion exchanged during mineral*
644 *melting may perturb the parallelism of the isotherms. Modified from Nielsen et al.*
645 *(2010).*

646

647 **Figure 2:** *Experimental pseudotachylytes and experimental data. (a) Evolution of*
648 *frictional traction τ vs. slip distance during experiments. The black in color segment*
649 *defines τ_{ss} for experiment S475. (b) Velocity function imposed to the samples in the*

650 *four experiments. (c) Photomosaic of BSE-FESEM images of experiment S475*
651 *performed at 30 MPa normal stress. The ~3 mm long embayment is in*
652 *correspondence of the biotite grain. (d) Pseudotachylyte of experiment HVR376 with*
653 *abundant angular clasts of quartz and few rounded clasts of plagioclase (andesine or*
654 *An₄₅ in composition) immersed in a Ca-rich glassy matrix. (e) Pseudotachylyte-host*
655 *rock (PST-HR) boundary of experiment HVR376 with evidence of melting and*
656 *dehydration (elongated vesicles) of biotite grains. A Fe-rich glassy matrix departs*
657 *from the biotite (c to e, BSE-FESEM images. PST, pseudotachylyte; Bt, Biotite; HR,*
658 *host rock; Pl, plagioclase; Qz, quartz).*

659

660 **Figure 3: Natural pseudotachylytes. (a) Drawing of the right lateral fault L05 (GPS**
661 *point N46 10' 348" E10 34' 864") with sample location (blue dots). The*
662 *compressional, neutral and extensional structural domains are evidenced by dark,*
663 *intermediate and light gray-colored areas, respectively. (b) Southern*
664 *pseudotachylyte-host rock (PST-HR) boundary from an extensional domain with two*
665 *embayments on biotite grains (Bt. The embayments are partially filled by a whitish*
666 *quartz-rich pseudotachylyte (sample L05-02). (c) Detail of the quartz-rich portion of*
667 *the pseudotachylyte in (b). The PST is formed by abundant quartz clasts welded by*
668 *devitrified glassy matrix and microlites of biotite and plagioclase (see also inset;*
669 *white arrow = Pl microlites). This ultrafine aggregate is interpreted as a clast-laden*
670 *melt filling the embayment. (d) Typical embayment in biotite at the PST-HR*
671 *boundary (see profile in Fig. 3b for location). The PST matrix at the contact with the*
672 *biotite grain includes microlites of biotite crystallized from the melt, indicative of*
673 *progressive melting of the biotite grain followed by crystallization of biotite microlites*
674 *during cooling and solidification of the melt. (e) Detail of the two PST-HR boundaries*

675 from a compressional domain. The northern boundary is smoother ($\omega_0 = 31 \mu\text{m}$) than
676 the southern one ($\omega_0 = 89 \mu\text{m}$) (sample L05-06). **(f)** Host rocks located to the north
677 (top, poorly damaged) and south (bottom, highly damaged) boundary of a neutral
678 domain (sample L05-08). **(g)** PST-HR boundaries of an injection vein (sample W05-
679 S01). IV, injection vein; Qz, quartz; Kf, K-feldspar; Pl, Plagioclase). (3b,e,g: Micro-
680 images collected with polarized petrographic microscope, plane polarized light; 3c,d:
681 BSE-FESEM images; 3f: FESEM-CL images).

682

683 **Figure 4:** Results of the Fast Fourier Transform (FFT) spectral analysis in
684 experimental and natural pseudotachylytes. **(a)** FFT spectra of the experimental
685 PST-HR boundaries (colored lines) with their respective ω_0 (= RMS, colored dots) vs.
686 PST-HR boundary length. The ω_0 values plot along the FFT spectra of their
687 respective PST-HR boundaries (Beeler, 2023). There are no substantial differences
688 between the spectra of the four experimental pseudotachylytes. **(b)** Natural faults:
689 FFT spectra of natural PST-HR boundaries (colored lines) with their respective ω_0 (=
690 RMS, colored dots). For displaying purposes, only one spectrum from each structural
691 domain is reported (See Supplementary Material SM2 for the entire dataset). The
692 ω_0 values plot along the FFT spectra of their respective PST-HR boundaries. The
693 FFT magnitude is higher in injection veins and extensional domain and lower in
694 neutral and compressional domains. **(c)** Slope of the FFT spectra regression line of
695 experimental PST-HR boundaries. There is no significant variation of the slope with
696 increasing dissipated power. **(d)** Slope of the FFT spectra regression line of natural
697 PST-HR boundaries of this study. As for the experiments, there is no clear
698 correlation between the slopes and the structural domains. The stress normal to the

699 *fault increases from extensional to compressive structural domains. Hence, in*
700 *natural faults, \dot{Q}_{ss} should also increase toward the right on the x-axis (see*
701 *discussion).*

702

703 **Figure 5:** *Grain-scale roughness of the PST-HR boundary in experimental and*
704 *natural pseudotachylytes (see Fig. 1 and Eqs. 1 and 2 for definition of ω_0 and λ_{ave}).*
705 *Sample locations and structural domains of the natural pseudotachylytes from the*
706 *northern PST-HR fault L05 (black circles, see also discussion about these*
707 *highlighted data) are reported in Fig. 3a. (a) λ_{ave} vs. ω_0 in experimental*
708 *pseudotachylytes. (b) λ_{ave} versus ω_0 in natural pseudotachylytes. (c) λ_{ave} as*
709 *function of \dot{Q}_{ss} in experimental pseudotachylytes. (d) λ_{ave} plotted for different*
710 *structural domains in natural pseudotachylytes from this study. (e) ω_0 as function of*
711 *\dot{Q}_{ss} in experimental pseudotachylytes. The solid black line is the distance*
712 *$z_{T=870^\circ C}/\sqrt{2}$. $T=870^\circ C$ corresponds to the calculated melting temperature $T_{m\,eff}$ for*
713 *biotite, derived from the depth of the embayments (see discussion); gray in color*
714 *dashed lines denote the standard deviation. The values of experimental \dot{Q}_{ss} are*
715 *reported in Table 1. (f) ω_0 estimates for injection veins and for the different structural*
716 *domains of fault veins in natural pseudotachylytes from this study.*

717

718 **Figure 6:** *Frictional power dissipation (\dot{Q}) range estimated for the fault segment L05*
719 *using the grain-scale roughness of the northern pseudotachylyte-host rock boundary*
720 *(gray dots) together with the calculated frictional power dissipation derived from the*
721 *experimental pseudotachylytes of this study (black dots) and of Di Toro et al. (2006)*

722 (diamonds). The estimate is based on the melting temperature of biotite derived from
723 the experimental pseudotachylytes ($870\text{ }^{\circ}\text{C} \pm 180\text{ }^{\circ}\text{C}$, Fig. 5d).

724

725 **Table 1:** Experimental data: target velocity, imposed normal stress, measured peak
726 and steady-state shear stress and calculated power per unit area. (*) experiment
727 published in Di Toro et al., 2006.

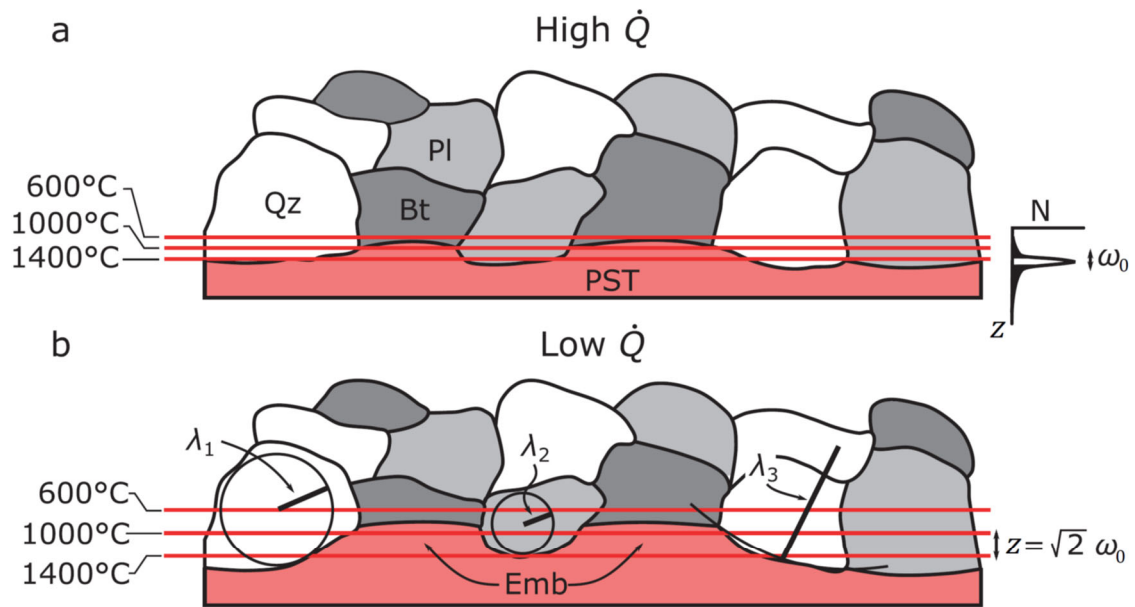
728

729 **Table 2:** Electron microprobe analysis (EMPA) of experimental pseudotachylytes:
730 (s.d. = standard deviation). Plagioclase and biotite compositions are from Di Toro and
731 Pennacchioni, 2004) and were obtained with the same electron microprobe and
732 working conditions.

733

734 **Table 3:** Grain-scale roughness parameters of the experimental and natural samples
735 analyzed in this study.

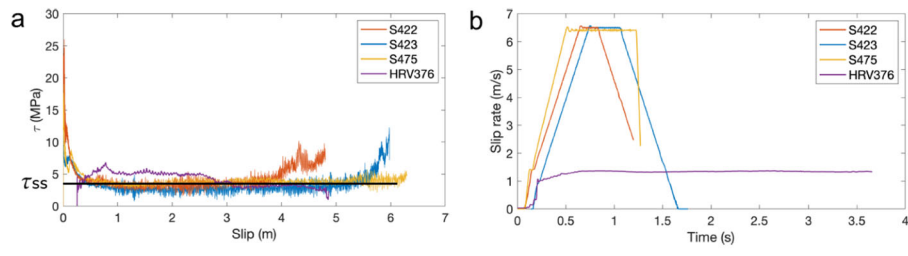
736



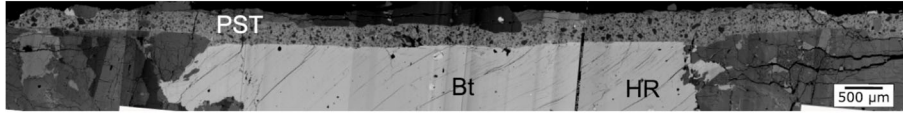
Lazari et al. Figure 1

737

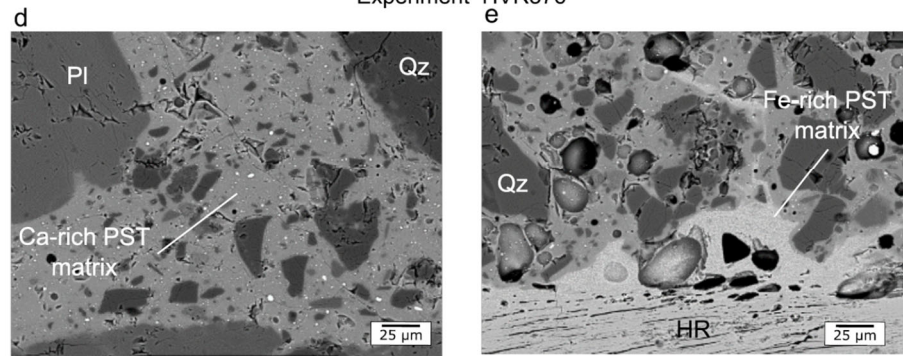
738



c Experiment S475



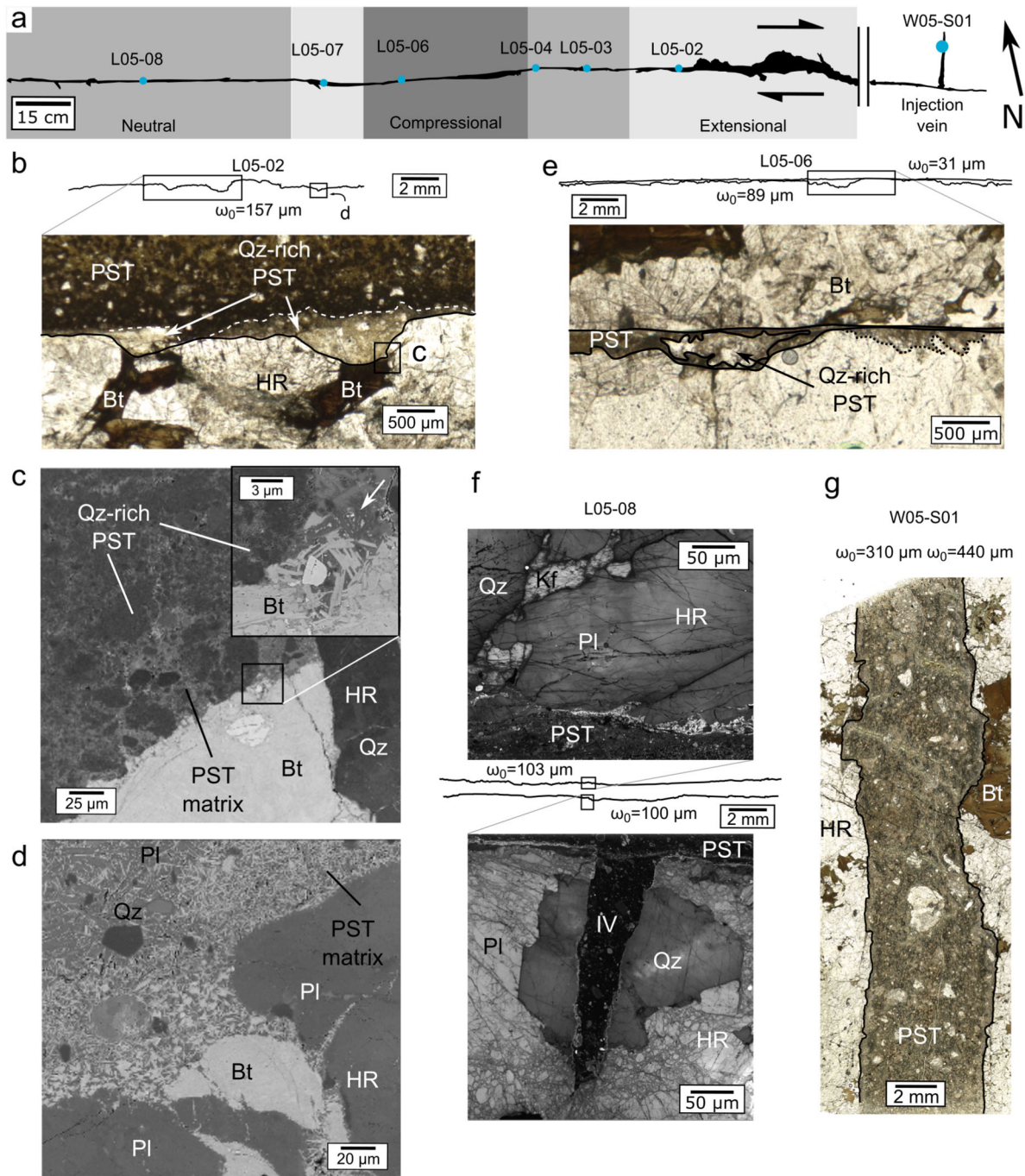
Experiment HVR376



739

Lazari et al. Fig. 2

740

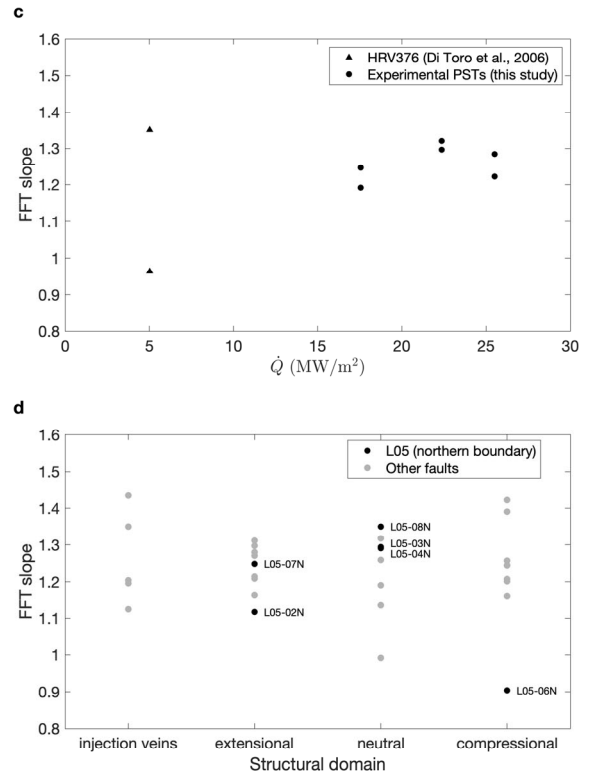
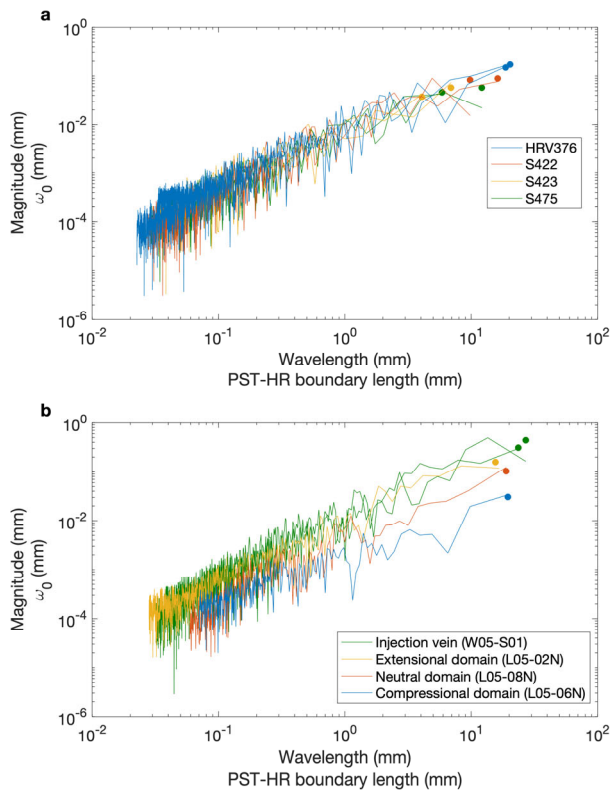


741

742

Lazari et al., Fig. 3

743

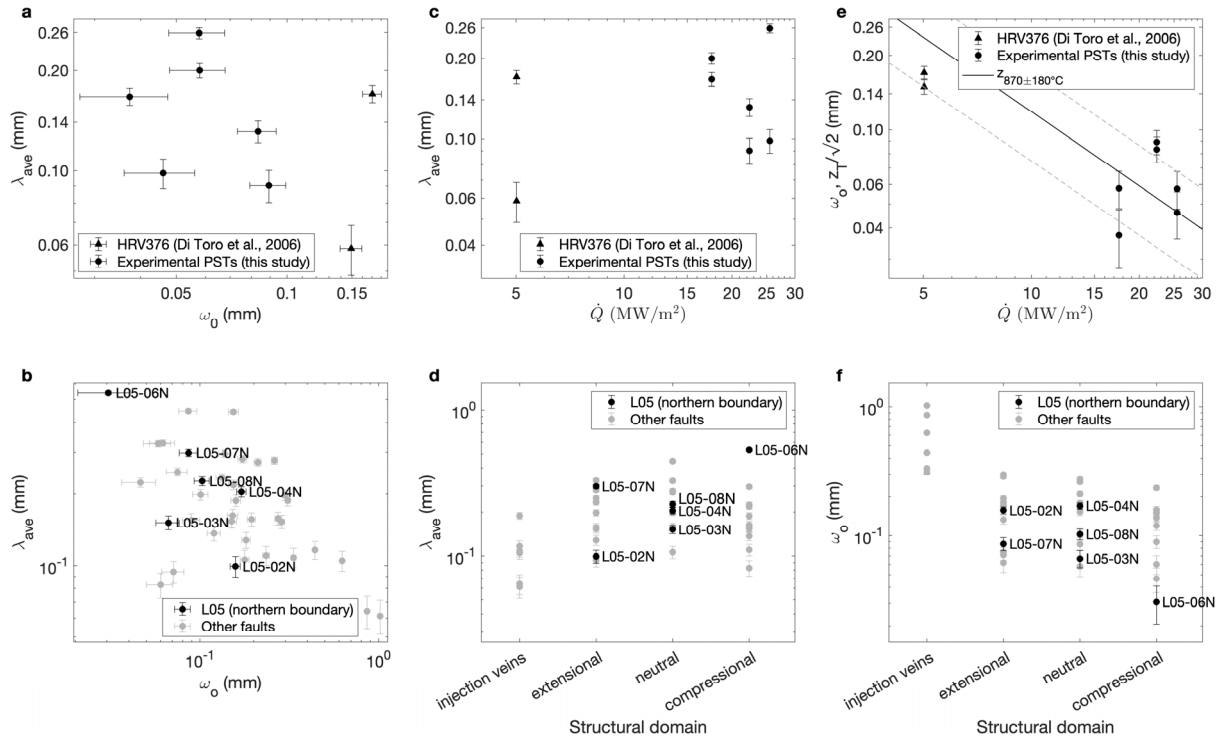


744

745

Lazari et al., Fig. 4

746

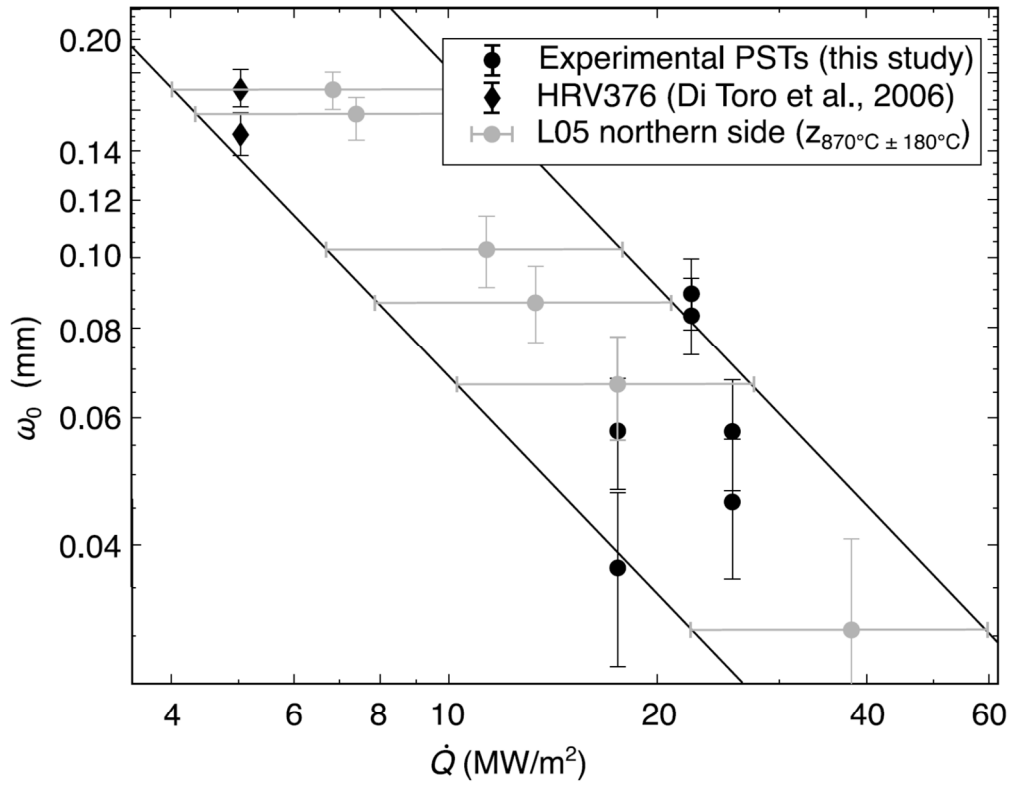


747

748

Lazari et al., Fig. 5

749



Lazari et al. Fig. 6

750

751

752 **Table 1:** Experimental data: target velocity, imposed normal stress, measured peak
 753 and steady-state shear stress and calculated power dissipation per unit area. (*)
 754 experiment published in Di Toro et al., 2006.

Experiment	Target velocity V_{eq_ss} (m s ⁻¹)	Normal stress σ_n (MPa)	Peak shear stress τ_p (MPa)	Steady-state shear stress τ_{ss} (MPa)	Power per unit area $\dot{Q}_{ss} = \tau_{ss} V_{eq_ss}$ (MW m ⁻²)
HRV376*	1.3	20	6.784	3.86	5.02
S422	6.5	40	26.04	3.44	22.36
S423	6.5	20	12.29	2.70	17.55
S475	6.5	30	19.05	3.92	25.50

755

756

757 **Table 2:** Electron microprobe analysis (EMPA) of experimental pseudotachylytes:
 758 (s.d. = standard deviation). Plagioclase and biotite compositions are from Di Toro and
 759 Pennacchioni, 2004) and were obtained with the same electron microprobe and
 760 working conditions.

	PST matrix (Ca-rich)		PST matrix (Fe-rich)		Plagioclase*		Biotite*	
	6 data	s.d.	2 data		15 data	s.d.	12 data	s.d.
SiO ₂	52.21	0.39	37.58		56.20	1.28	35.45	0.19
TiO ₂	1.16	0.07	2.73		0.02	0.01	2.55	0.50
Al ₂ O ₃	22.11	0.30	17.82		26.96	0.94	17.33	0.20
FeO _{tot}	7.71	0.27	21.53		0.38	0.29	20.59	0.42
MnO	0.26	0.04	0.59		0.12	0.11	0.01	0.01
MgO	3.92	0.20	9.73		0.02	0.01	9.04	0.46
CaO	4.84	0.19	0.08		9.33	1.02	0.03	0.04
Na ₂ O	2.88	0.18	0.62		5.98	0.62	0.08	0.02
K ₂ O	4.18	0.14	8.27		0.53	0.22	9.33	0.44
Tot	99.26	0.11	98.94		99.54	0.76	94.43	0.88

761 *Data from Di Toro and Pennacchioni (2004)

762

763 **Table 3:** Grain-scale roughness parameters of the experimental and natural samples

764 analyzed in this study.

Sample	λ_{ave} (mm)	λ_{ave} deviation (mm)	ω_0 (mm)	ω_0 deviation (mm)	FFT slope (adimen.)	FFT intercept (mm)	\dot{Q}_{ss} (MW m ⁻²) or structural domain
HRV376 top	0.1702	0.1714	0.1703	0.1768	0.9639	-5.2620	5.020
HRV376 bot	0.0586	0.0511	0.1493	0.1463	1.3516	-4.5176	5.020
S422 top	0.1312	0.1540	0.0833	0.0772	1.3211	-4.6116	22.36
S422 bot	0.0903	0.0796	0.0892	0.0865	1.2966	-5.1414	22.36
S423 top	0.1671	0.1398	0.0374	0.0341	1.2463	-4.7004	17.55
S423 bot	0.2000	0.2039	0.0579	0.0578	1.1918	-5.2449	17.55
S475 top	0.0983	0.0538	0.0461	0.0481	1.2846	-4.7907	25.50
S475 bot	0.2590	0.2705	0.0577	0.0606	1.2220	-5.1841	25.50
A1E	0.1047	0.1319	0.6252	0.6059	1.4345	-3.7856	injection vein
A1W	0.1080	0.1357	0.3346	0.3595	1.2042	-4.3912	injection vein
A02-02N	0.2474	0.2072	0.0747	0.0797	1.2144	-5.4969	neutral
A02-02S	0.0941	0.0999	0.0710	0.0702	1.2975	-4.4707	neutral
A02-04N	0.1364	0.1522	0.1197	0.1156	1.2074	-5.2784	compressional
A2E	0.0642	0.0641	0.8621	0.8853	1.1964	-4.4267	injection vein
A2W	0.0613	0.0831	1.0217	1.0851	1.3500	-4.5118	injection vein
A4N	0.2769	0.2175	0.2613	0.2588	1.3176	-5.5750	neutral
A4S	0.1578	0.1396	0.2729	0.2554	1.1910	-4.9211	neutral
A5N	0.1277	0.1259	0.1812	0.1848	1.2490	-5.4868	extensional
A5S	0.2333	0.2149	0.1331	0.1431	1.2801	-5.2390	extensional
A7N	0.1625	0.1625	0.1525	0.1396	1.2450	-5.4098	compressional
A7S	0.2957	0.1966	0.1374	0.1376	1.2016	-5.5869	compressional
L05-02N	0.0992	0.1138	0.1577	0.1601	1.1171	-4.8767	extensional
L05-03N	0.1515	0.1470	0.0666	0.0643	1.2943	-5.0969	neutral
L05-04N	0.2039	0.2184	0.1707	0.1552	1.2910	-5.0811	neutral
L05-04S	0.1059	0.1073	0.1780	0.1750	1.2922	-4.3669	neutral
L05-06N	0.5323	0.2699	0.0307	0.0341	0.9041	-6.3854	compressional
L05-06S	0.1553	0.2183	0.0895	0.0773	1.1598	-5.1893	compressional
L05-07N	0.2979	0.2356	0.0864	0.0816	1.2482	-4.8399	extensional
L05-07S	0.3271	0.2671	0.0619	0.0584	1.1624	-4.6570	extensional
L05-08N	0.2260	0.1991	0.1027	0.0955	1.3502	-5.4975	neutral
L05-08S	0.1982	0.1682	0.1008	0.0945	1.2591	-5.6017	neutral
L09-01aN	0.1527	0.1740	0.2870	0.2872	1.2703	-4.9312	extensional
L09-01aS	0.1974	0.1759	0.2986	0.3298	1.2092	-4.9801	extensional
L09-02aN	0.1877	0.1522	0.1589	0.1578	1.2573	-5.1675	compressional
L09-02aS	0.2178	0.2046	0.1540	0.1408	1.2445	-5.3854	compressional
L09-02bN	0.2230	0.2191	0.0464	0.0429	1.1145	-5.9520	compressional
L09-02bS	0.0827	0.0883	0.0602	0.0544	1.2487	-4.8847	compressional

L09-03aN	0.2723	0.3508	0.2109	0.1974	1.1890	-5.6802	neutral
L09-03aS	0.4446	0.2220	0.1541	0.1720	0.9918	-5.5594	neutral
L09-03bN	0.3253	0.2289	0.0582	0.0554	1.1462	-5.5622	neutral
L09-03bS	0.4476	0.4125	0.0859	0.0798	1.1353	-5.0145	neutral
W05-S01E	0.1162	0.1509	0.4403	0.4540	1.3453	-4.6167	injection vein
W05-S01W	0.1882	0.1789	0.3100	0.2837	1.1248	-4.3834	injection vein
W05-S04N	0.1565	0.1735	0.1941	0.1963	1.2653	-5.5436	extensional
W05-S04S	0.2812	0.2011	0.1728	0.1752	1.3115	-4.5132	extensional
W09-S01N	0.1100	0.1293	0.2344	0.2318	1.3903	-4.8358	compressional
W09-S01S	0.1537	0.1201	0.1502	0.1541	1.4221	-5.1237	compressional

765

766

767